

Influence of ionization and cumulative effects on laser-induced crystallization in multilayer dielectrics

Ruben Ricca^{1,*}, Victor Boureau², and Yves Bellouard¹

¹Galatea Laboratory, STI/IEM, Ecole Polytechnique Fédérale de Lausanne (EPFL), 1015 Lausanne, Switzerland

²Interdisciplinary Center for Electron Microscopy, Ecole Polytechnique Fédérale de Lausanne (EPFL), 1015 Lausanne, Switzerland



(Received 14 December 2023; accepted 21 May 2024; published 12 June 2024)

Crystallization of amorphous layers has been demonstrated under various radically different laser-exposure conditions, including continuous wave (cw) and pulsed lasers. Here, we investigate the specific role of ionization in the crystallization of dielectric SiO₂/SiN_x multilayers. This choice is motivated by the technological relevance of the interaction between lasers and a multilayer thin films system in distributed Bragg reflectors. Specimens were exposed to both femtosecond laser pulses, triggering bulk ionization thanks to nonlinear absorption processes, and a cw infrared laser, whose photon energy is lower than the dielectrics band gap, resulting in a purely linear absorption mechanism rather than ionization. While femtosecond laser exposure leads to the formation of Si nanocrystals homogeneously confined within the focal volume and extending to adjacent SiN_x layers, cw laser exposure leads to the formation of polymorphic crystalline phases of Si₃N₄ in the SiN_x layers, along with a Si phase *within* the SiO₂ layers, which otherwise remain amorphous.

DOI: [10.1103/PhysRevMaterials.8.063402](https://doi.org/10.1103/PhysRevMaterials.8.063402)

I. INTRODUCTION

The optical, mechanical, and thermal properties of a material are intimately linked to its crystallographic structure. For fixed atomic compositions, polymorphs of the same compound can have radically different physical properties. A vivid illustration is to compare the mechanical properties of diamond and graphite. While both are polymorphic phases of carbon, graphite's Young modulus is about 100 times lower than diamond. In the micromanufacturing context, locally tailoring the material structural states enables functional devices in which multiple phases of the same material coexist [1,2]. For that purpose, laser-induced crystallization not only provides a means to achieve “material phase” engineering with micronscale resolution, but also a means to achieve extreme temperature and pressure dynamical range and conditions, thanks to a *rapid* and *localized* energy transfer in the material.

In conventional laser annealing, i.e., when no ionization takes place, linear photon absorption mechanisms govern and provide a rapid, localized, and effective means to transfer energy in the form of heat to the material, sufficiently high to induce phase transformation and structural reorganization, such as crystallization. The end product of the annealing is similar to a classical phase transformation as obtained through a rapid temperature-driven phase change. Laser-induced crystallization in dielectrics was also reported after ultrashort laser-pulse exposure, during which nonlinear absorption processes triggered by multiphoton ionization are taking place [3–7]. In this context, we reported crystalliza-

tion occurring at timescales where no heat diffusion occurred out of the focal zone, and in exposure conditions driven by single pulse dynamics, corresponding to low-repetition-rate conditions [8–10]. These observations, related to the extreme brevity of the pulses (less than 500 fs), suggest different physical mechanisms leading to crystallization than what is usually observed with laser annealing with longer pulses and/or continuous-wave (cw) exposure, likening observations made in silicon [11–13].

The present study explores laser-induced crystallization phenomena in dielectrics through three different laser-exposure modalities. Specifically, we investigate the role of laser-induced ionization as a precursor to crystallization processes by comparing it to a purely temperature-driven process, in which no ionization is taking place, due to the low photon energy and irradiance level. In addition, we consider the case where the temperature gradually builds up through successive and cumulative femtosecond laser pulse exposure fired at a rate that is sufficiently high to prevent the occurrence of thermal relaxation in between pulses and for heat to diffuse away from the laser focus (illustrated in Fig. 1). The objective is to highlight fundamental differences between laser-annealing modalities, studying ionizing versus nonionizing exposure conditions.

The investigation considers multilayer thin films as a case study. This choice of substrate is motivated by our previous experimental observations that offer a starting point for the present study [9,10], but also by the practical importance of distributed Bragg reflectors in a variety of optical applications and the need to better understand their behavior under intense laser-exposure conditions.

II. MATERIALS AND METHODS

The samples consist of a multilayer thin film stack, made of alternating SiO₂ and SiN_x. The individual layer thicknesses are consistent with a $\lambda/4$ distributed Bragg reflector (DBR)

*ruben.ricca@alumni.epfl.ch

Published by the American Physical Society under the terms of the Creative Commons Attribution 4.0 International license. Further distribution of this work must maintain attribution to the author(s) and the published article's title, journal citation, and DOI.

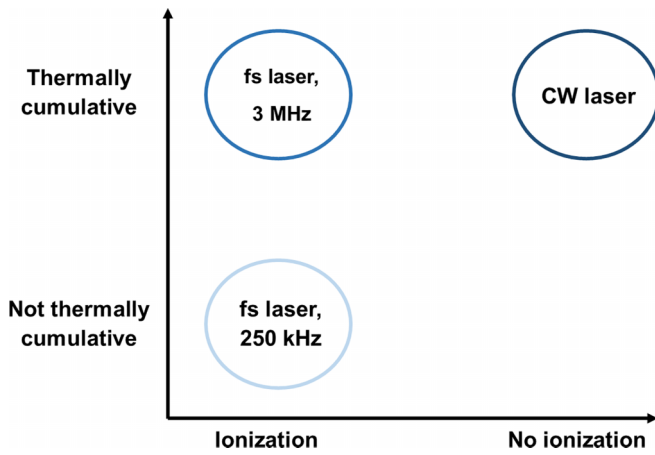


FIG. 1. Summary of the three laser-exposure regimes considered in this study: a laser source triggering nonlinear absorption effects and no thermal accumulation effects (femtosecond laser, 250 kHz); the same nonlinear source, but at higher pulse repetition frequencies (3 MHz), enabling conditions for pulse-to-pulse thermal effects; and a continuous-wave laser source emitting in the infrared, where the absorption mechanism is linear and nonionizing, and the laser-matter interaction is purely thermal.

grating design [14], with the SiO_2 layers having a thickness of 119 nm and the SiN_x layers of 87 nm. Note that the upper layers' thicknesses are not as homogeneous as the lower ones due to roughness induced by the deposition process. Thirteen pairs of layers were deposited, resulting in a total multistack thickness of 2.68 μm . The layers were deposited on a fused silica substrate (4 inch wafer) by plasma-enhanced chemical vapor deposition (PECVD) (from Oxford Plasmalab), at a deposition temperature of 300 $^\circ\text{C}$. The wafer was then diced into smaller samples. The layers after deposition are amorphous as verified with Raman spectroscopy (Horiba Jobin-Yvon LabRam HR). The SiN_x layers are effectively slightly richer in silicon than their stoichiometric design formulation Si_3N_4 . To reflect this difference, we use the more general SiN_x as notation, with $x \approx 0.5$. When dealing with crystalline compounds that are more in line with the stoichiometric proportions, the notation Si_3N_4 will be adopted.

Two laser sources were used in this study: a femtosecond fiber ytterbium-based laser (Yuzu from Amplitude) emitting at 1030 nm and operated at two different repetition rates of 250 kHz and 3 MHz, and a continuous-wave midinfrared CO (Diamond C-55-5 from Coherent) laser emitting photons at 5 μm . The pulse duration of the femtosecond laser source was 270 and 300 fs, measured at 250 kHz and 3 MHz, respectively. The pulse broadening at 3 MHz has no effect on the number of photons required for ionizing the material, and hence can be neglected in the rest of the discussion.

The femtosecond laser beam was focused on the sample using a microscope objective (Microspot from Thorlabs, NA 0.4), producing a beam spot of about 2 μm , while the CO laser beam was focused using a ZnSe lens (focal length 35 mm), resulting in a beam diameter of approximately 300 μm . In both cases, the laser is scanned over the specimen surfaces using translation stages to achieve a given exposure dose over a predefined area.

For the low pulse energies considered here (<150 nJ), yielding a little less than 10^{13} GW cm^{-2} , we did not observe

evidence of cumulative effects at 250 kHz compared to lower repetition rates that yielded similar results.

Based on the literature data, Si_3N_4 has up to 30% higher heat capacity than SiO_2 and an order of magnitude higher conductivity (typically between 10 to 30 times higher). The estimated diffusivity of SiO_2 ranges from ~ 0.78 to ~ 0.9 mm^2/s and the one of Si_3N_4 is from ~ 6.2 up to ~ 12 mm^2/s . Taking our spot size, at 250 kHz (i.e., 4 μs between pulses), the “diffusion surface” is at least 10 times bigger than the spot area for Si_3N_4 and slightly bigger than the spot size for SiO_2 . Adopting a rule of mixture for estimating the average diffusion surface (considering that thin films have about the same thickness), a rough estimate gives about three to six times more than the spot surface.

The complex refractive indexes k of SiO_2 and Si_3N_4 at 5 μm are $k_{\text{SiO}_2} = 0.00076$ and $k_{\text{Si}_3\text{N}_4} = 0.00445$ [15], respectively. The absorption coefficient α ($\alpha = 4\pi k/\lambda_0$) indicates that the nitride phase is about six times more absorptive than the silica one ($\alpha_{\text{SiO}_2} = 1.91 \times 10^3$ m^{-1} versus $\alpha_{\text{Si}_3\text{N}_4} = 11.18 \times 10^3$ m^{-1}).

At 5 μm , the photon energy is 0.248 eV, which is an order of magnitude lower than the band gap of both layer materials considered here. Furthermore, the power density is, at most, 180 kW cm^{-2} . Hence, no ionization can take place in such exposure conditions and the laser-matter interaction is exclusively governed by heat transfer.

Material characterization was performed by transmission electron microscopy (TEM), using a Thermo Fisher Scientific Talos F200S operated at 200 kV, under bright-field (BF) and dark-field (DF) TEM imaging conditions. Selected area electron diffraction (SAED) and energy-dispersive x-ray spectroscopy (EDS) scanning-TEM (STEM) techniques were used to unravel the crystalline structures of selected areas and to analyze variations in composition. 100-nm-thick cross section lamellas of the samples were realized by a focused ion beam (FIB) (Zeiss NVision 40 dual-beam SEM/FIB) to observe the exposed sections in scanning electron microscopy (SEM) mode and for transfer to the TEM. Scanning precession electron diffraction (SPED) was also realized, using an Astar system installed on a FEI Tecnai Osiris TEM, for local phase and orientation mapping of the crystallites in the specimen [16,17]. The Astar-SPED measurements were conducted at 200 kV, with a beam current of 12 pA, a precession speed of 100 Hz at an angle of 0.6 $^\circ$, a dwell time of 20 ms, and a step size of 3.75 nm.

III. RESULTS

A. Femtosecond laser exposure at low and high repetition rate

In [9], we discussed the low-repetition-rate case of femtosecond laser exposure of $\text{SiO}_2/\text{SiN}_x$ specimens. Highlights of this study are reproduced in Figs. 2(a) and 2(b), for direct comparison with the case of high-repetition-rate exposure (250 kHz, a scan speed of 1 mm s^{-1} , and a pulse energy of 78 nJ, resulting in an exposure dose of 2.49 kJ cm^{-2} and a fluence of 4.97 J cm^{-2} per pulse). The images show a cross section of a modified zone, perpendicular to the scanning direction of the laser. The \mathbf{k} vector indicates the laser propagation direction. In Fig. 2(a), the laser-modified area stretches a few microns away

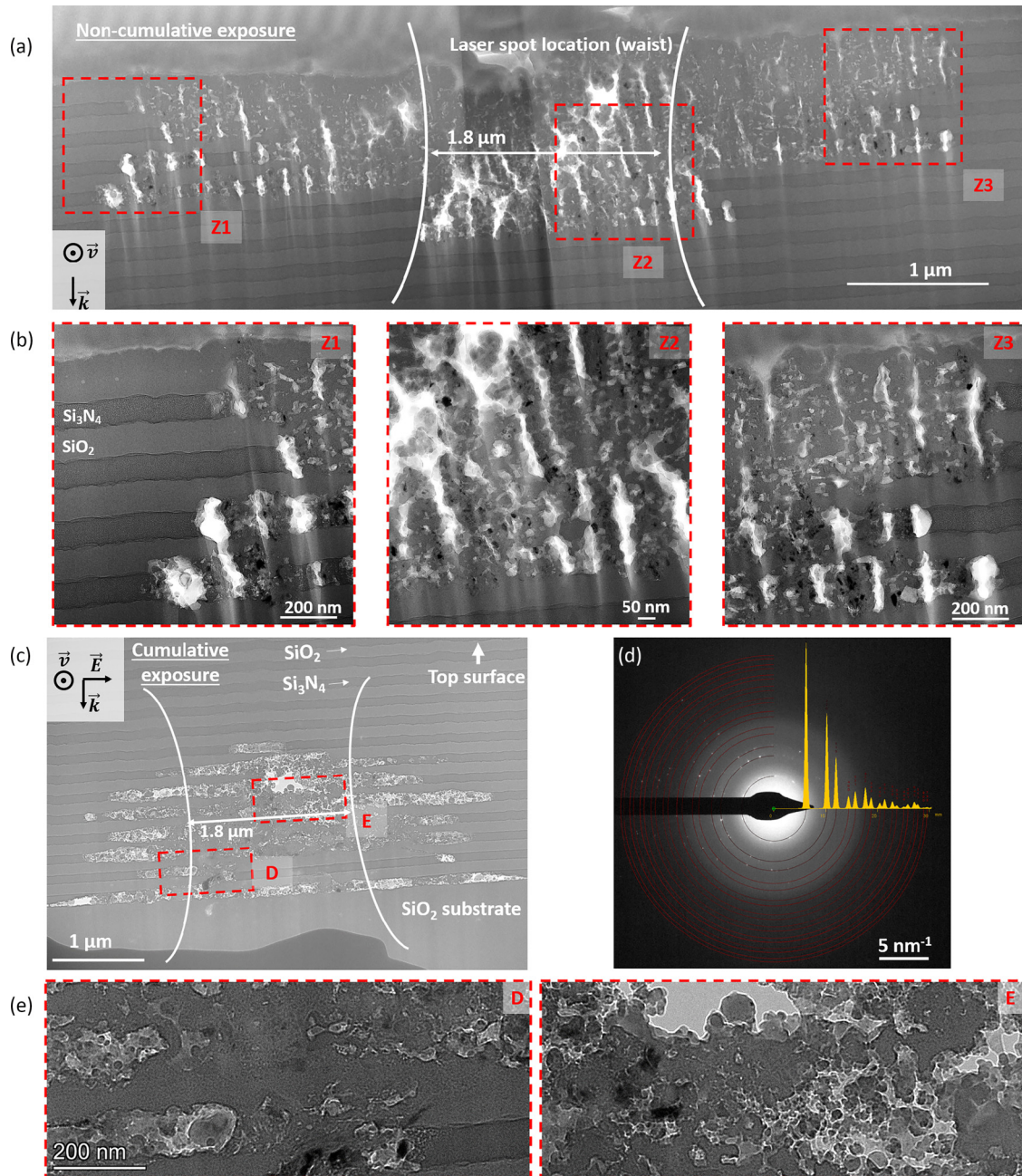


FIG. 2. Case of femtosecond laser exposure of SiO₂/SiN_x multilayers, (a),(b) in a noncumulative regime (repetition rate 250 kHz, 78 nJ pulse energy) and (c)–(e) in a cumulative regime (repetition rate 3 MHz, 16 nJ pulse energy). (a) BF-TEM image. The SiN_x layers appear darker. (b) Higher magnification BF-TEM images of regions A, B, and C [highlighted in red in (a)], showing the distribution of the silicon crystallites within the laser-affected area. (c) BF-TEM image. Besides a central area (indicated by the approximate location of the beam waist), showing higher levels of intermixing, most modifications are confined to the high-index SiN_x layers. (d) SAED pattern originating from the modified area, evidencing the presence of crystallites of Si diamond crystal with no preferential orientation. (e) Higher magnification BF-TEM images of areas D and E, as highlighted in red in (c). Images (a) and (b) have been reproduced and modified from [9], with permission from the American Institute of Physics (AIP).

from the beam-waist focus (indicated in white in the image). Voids are visible, somewhat periodically spaced, and initially confined in the SiN_x layers as suggested by observations away from the laser waist. Higher-magnification BF-TEM images shown in Fig. 2(b), corresponding to locations Z1, Z2, and Z3 of Fig. 2(a), indicate the occurrence of intermixing between layers within most of the laser-affected area, excluding the edges, where modifications remained confined in the SiN_x

layers. In the region where intermixing occurred, which is mostly located within the waist of the laser, both the location and dimensions of the voids' distribution are less homogeneous. Pure silicon crystallites with dimensions lower than 50 nm [shown by a darker contrast in Figs. 2(a) and 2(b)] are observed spread around the modified volume, without a clear preferential distribution within the layers in the middle of the laser-affected zone, but strictly confined in the SiN_x

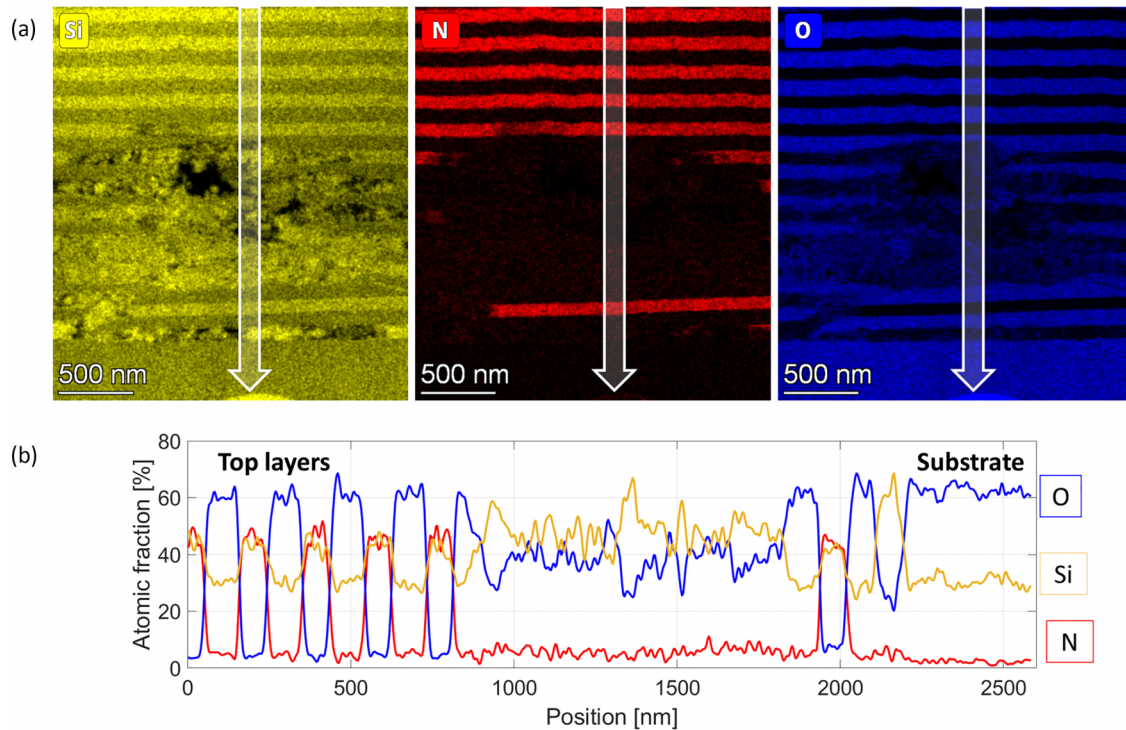


FIG. 3. Element mapping (EDS) of Si, N, and O atoms across the laser-affected area, indicating a redistribution of both silicon and oxygen atoms, and the depletion of nitrogen (a). The white arrows represent the profile's location for atomic species composition shown in (b) as a function of depth. The width of the arrow represents the integration width of the profile.

layers in the peripheral zones. This suggests that conditions for crystallization are first met in the SiN_x layers by dissociation of the nitrogen. Crystallites are mixed within layers in the beam-waist location.

Let us now consider the high-repetition-rate case, corresponding to a thermally cumulative regime. In this regime, the time between pulses was chosen such that the average temperature in the waist gradually increases after each pulse and diffuses away from the beam waist until a steady-state average temperature is reached [18]. To fulfill this condition, a repetition rate of 3 MHz was selected. To limit the size of the ionized volume, the pulse energy of 16 nJ was chosen just above the nonlinear absorption threshold. Finally, the scan speed of 10 mm s^{-1} results in an exposure dose of 0.61 kJ cm^{-2} , about four times lower than in the low-repetition-rate case, and a fluence of 1.02 J cm^{-2} per pulse. Higher exposure dose values, similar to the one used for the low-repetition-rate case (2.49 kJ cm^{-2}), were deemed excessive as they invariably resulted in the removal of the layers, and are therefore not of interest for this study. The scanning conditions, namely, the scanning and the laser propagation directions, are the same as for the previous sample, as indicated in the TEM cross sections of Figs. 2(c) and 2(e).

The total thickness of the multilayers makes it difficult to focus the laser at a precise location within the stack. Here, the modifications were concentrated at the lower section of the multilayer stack, as visible in Fig. 2(c). The center part of the modified zones displays strong intermixing, as shown in Fig. 3. Outside the center of the laser-affected zone, damaged zones are found in the SiN_x layers, which is the layer having the highest thermal conductivity (the thermal conductivity of

SiN_x is in the range 7.5 to 30 times higher than SiO_2 [19,20]). Unlike in the case of a lower repetition rate, there is no evidence of periodic arrangements of the modifications and the central region is comparatively more compact and denser.

The SAED pattern of the laser-affected area is shown in Fig. 2(d), evidencing the presence of crystallites with no preferential orientation. The diffraction pattern can be associated with a cubic diamond Si phase, as shown by the simulation of the Bragg diffraction intensities overlapped on the experimental SAED. A quantitative comparison of interplanar distances measured in the SAED pattern of Fig. 2(d) (with reference values for Si diamond crystal phase [21]) is provided in Table SI in the Supplemental Material [22]. Figure 2(e) shows higher magnification BF-TEM images of areas D and E, highlighted in red in Fig. 2(c), in which the presence and distribution of crystallites is revealed as darker areas.

The EDS maps (Fig. 3) show the elemental distribution of Si, O, and N within the same cross section of a laser-affected zone [Fig. 3(a)] and the atomic fraction of each species across the depth of the multilayer stack [Fig. 3(b)]. The nitrogen concentration drops dramatically in the modified areas, even though they are located within the material, $1 \mu\text{m}$ below the surface. Its atomic concentration falls below 10% in the whole area, indicating a removal of N from the laser-affected volume: a simple redistribution of the N atoms would have led to a homogeneous concentration in the range of 25–30%. A combination of homogeneous redistribution of N atoms within the modified volume with the formation of volatile gas molecules escaping through porous zones is foreseen as an explanation of this phenomenon.

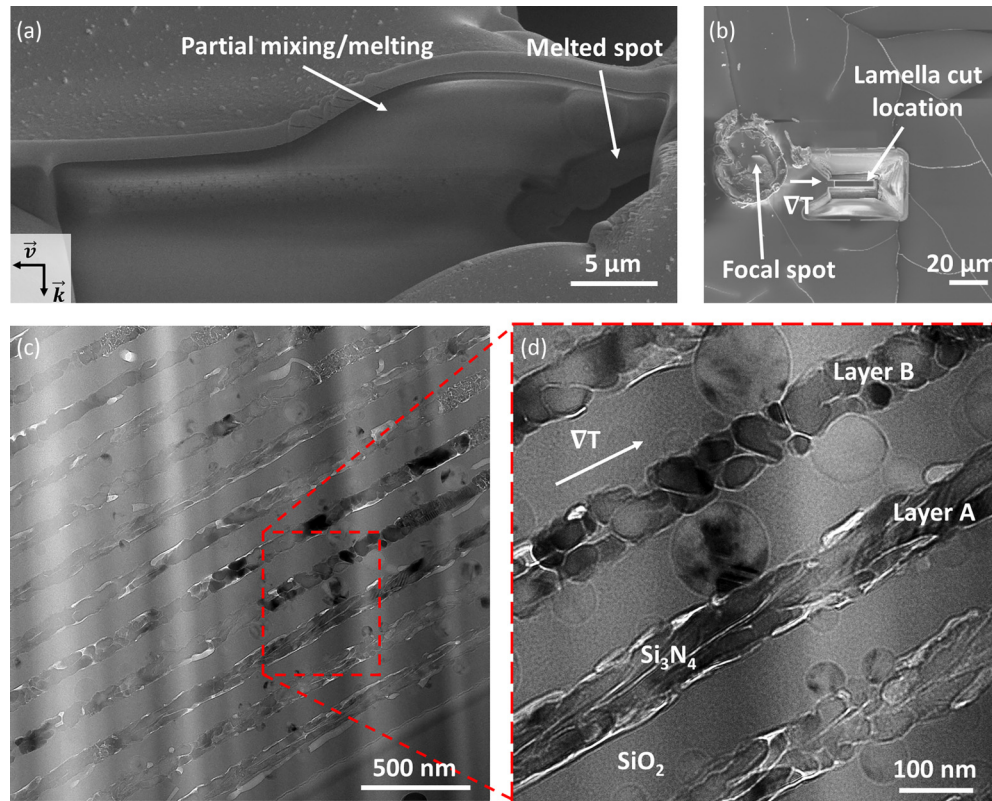


FIG. 4. (a) SEM image of a material cross section after exposure to a cw mid-IR CO laser emitting at $5\ \mu\text{m}$. The nature of the laser-matter interaction with the dielectrics layers is exclusively thermal, as the photon energy is not sufficient to ionize the matter. The layered structure is preserved until the ablation crater as a result of the fast melting and vaporization of the material directly under focus. Around the crater, the layers' structure is disrupted and the atomic species are fully intermixed, as a result of the resolidification process. This case is helpful to investigate how the layers evolve under a pure thermal load. (b) SEM image of the surface of the layered material showing the ablation crater and the location of the specimen cross section for TEM analysis. (c) BF-TEM image of the multilayers exposed to CO laser radiation, showing widespread crystallization over the full multilayer stack thickness. (d) Higher magnification of a portion of the lamellas, with polycrystalline structures in place of the SiN_x layers and spherical crystallites growing inside the otherwise amorphous SiO_2 layers.

On the contrary, Si and O species remain in high concentrations and are redistributed around the laser-affected volume, with localized, high-concentration Si nanoparticles observed at the location of what appears to be crystallites (as unraveled by the SAED analysis). The observation of these crystallites is similar to what has been reported in [9] in the case of the low-repetition-rate sample.

Comparing TEM images of low- and high-repetition-rate specimens, we formulate the following observations: first, increasing the repetition rate reduces the intermixing homogeneity outside of the focal spot location and promotes a preferential modification of the nitride layers. Second, the high-repetition-rate specimen does not show evidence of self-organization. Third, in both cases, crystallites are randomly distributed and are of comparable dimensions (diameter $\leq 50\ \text{nm}$). Fourth, the extension of both modified areas in longitudinal and transversal directions is similar, spanning between 1.1 and $1.6\ \mu\text{m}$ (transversal) versus 6.0 and $5.3\ \mu\text{m}$ (longitudinal), for the low- and high-repetition-rate cases, respectively. It should be highlighted that both the pulse energy and the deposited energy are much smaller in the case of high-repetition-rate exposure. Consequently, the volume in which nonlinear absorption occurs is an order of magnitude smaller than the low-repetition-rate case. Hence, the presence of such

a large modified volume can solely be attributed to a thermal increase and heat diffusing away from the laser-affected area. These observations highlight that self-organization can clearly be attributed to the high field strength (higher energy in the low-repetition-rate case) and that crystallites are primarily occurring to given thermal conditions and do not seem to be influenced by the field strength.

To summarize, femtosecond laser exposure at a repetition rate of $250\ \text{kHz}$ resulted in the formation of Si crystallites distributed across the modification volume, together with an intermixing of silicon and oxygen atoms, with a concentration of the modifications in the nitride layers outside of the focal spot location. In contrast, femtosecond laser exposure at a higher repetition rate of $3\ \text{MHz}$ shows that the SiN_x layers are even more affected by the laser exposure and selectively modified. Both cases resulted in the depletion of most of the native nitrogen from the affected areas, but self-organization was observed only in the low-repetition-rate cases.

B. CO laser exposure

The specimen was also exposed to a cw mid-IR laser (CO, $5\ \mu\text{m}$) according to two different modalities: either by scanning the laser over its surface (scanning speeds between

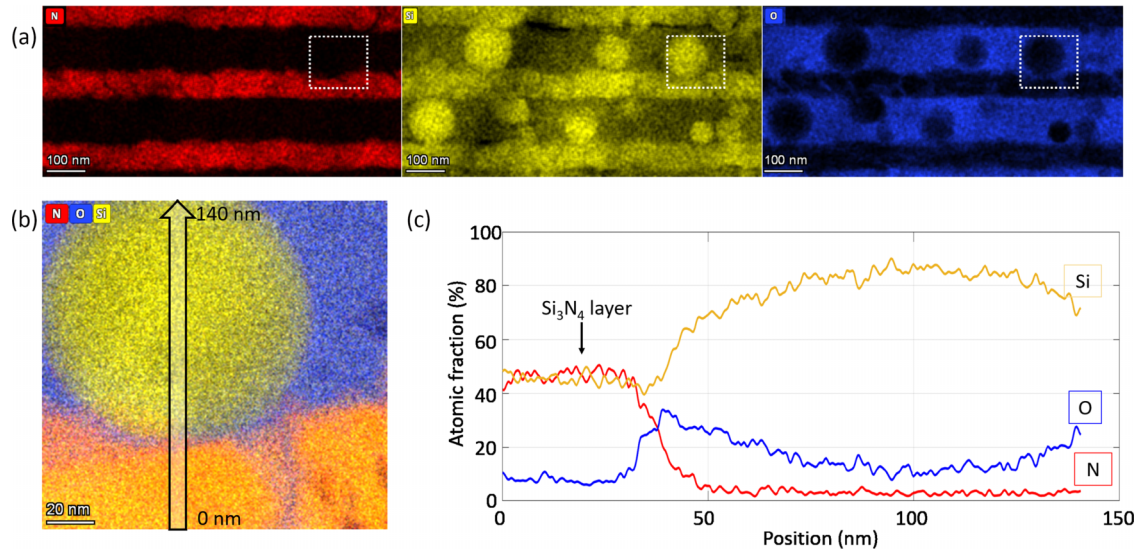


FIG. 5. (a) EDS elemental mapping of N, Si, and O atoms across the sample exposed to the CO laser. (b) EDS composite elemental map at the interface between an amorphous SiO_2 layer including a Si crystallite and a crystalline Si_3N_4 layer, at the location of the white rectangle depicted in (a). (c) Profile of the atomic fraction of N, O, and Si, along the black arrow in (b).

$25 \mu\text{m s}^{-1}$ and 4mm s^{-1}) or by irradiating a single spot. Although it was not possible to directly measure the energy of the laser beam due to limitations on the experimental setup, we were able to control the power percentage and use it as a basis for comparison between different experimental conditions. By varying the power percentage, it was possible to explore how different levels of power affect the multilayer samples. A power percentage set value of 100% corresponds to an output of 40 W.

Under these conditions, laser irradiation in scanning mode resulted in spaced, melted dots along the writing line, with diameters of approximately $30 \mu\text{m}$. Figure 4(a) shows the cross section of one of these molten spots, cut and exposed along the writing direction. Here, the power was set at 15% (hence a maximal power of 6 W), the scan speed was $40 \mu\text{m s}^{-1}$, and the scan length was 6 mm. Due to the extreme heating, part of the layers melted, resulting in a relatively deep crater. Outside of the crater, the layers' structural integrity is largely preserved. However, the layers' microstructure is still affected, as illustrated by the dark spots visible within the layers in Fig. 4(a), which correspond to laser-induced crystallites.

Laser exposure in single spot mode, at 25% of the power (hence a maximal power of 10 W) and for a duration of 10 s, resulted in the creation of an ablation crater of approximately $40 \mu\text{m}$ of diameter, with the presence of cracks around the laser-affected area, which are due to temperature-induced stress following the irradiation and the rapid cooling of the material. A cross-section lamella of a sample exposed under these conditions was cut out for TEM observation 25–45 μm away from the crater's edge, as shown in Fig. 4(b).

A BF-TEM image of this lamella is shown in Fig. 4(c), showing how the laser affects the totality of the layers of the stack, without evidence of preferential modification of a specific layer. A higher magnification BF-TEM image [Fig. 4(d)] shows the growth of crystallites inside the SiN_x layers with some of the grains (layer A in the figure) elongated along the

length of the layers. This orientation suggests a preferential growth direction that follows the thermal gradient. Layer B shows grains with a more isotropic shape and that are more evenly distributed.

Within the SiO_2 layers, spherical crystallites of varying size testify to nucleation processes occurring at the interface between the two materials.

EDS chemical mapping of the modified area is visible in Fig. 5(a), with three images of the same cross section detailing the atomic distribution of N, Si, and O. The chemical integrity of the SiN_x layers is generally preserved, as no elemental intermixing is observed between the layers, and the nucleation and growth of a heterogeneous phase of silicon crystal inside the SiO_2 layer is confirmed.

Figure 5(b) [magnified area indicated by white rectangles in Fig. 5(a)] evidences a decrease of oxygen along with an increase of silicon in spherical crystallites present in the SiO_2 layers and the presence of oxygen at the grain boundary between these crystallites and the SiN_x layers. The elemental distribution along a vertical line, indicated by the black arrow, is plotted in Fig. 5(c) and confirms these observations.

To analyze the nature and the phase of the different crystallites, a scanning precession electron diffraction configuration of the TEM was used. This method allows for scanning the specimen with a small electron probe, while recording the pseudo-kinematical diffraction patterns with a camera, at each location in the specimen. The processing (using the ASTAR software suite [16]) of each diffraction pattern allows for the determination of the crystals phases and orientations distribution in the specimen, with, in our case, a spatial resolution of 8 nm. The Astar-SPED results are presented in Fig. 6, measured at a location in the vicinity of Fig. 4(c), with the BF-TEM image of this specific area shown in Fig. 6(a). Another analysis taken at a different location of the lamella is presented in Fig. S1 in the Supplemental Material [22] and shows analogous results. Figure 6(b) is the correlation map of

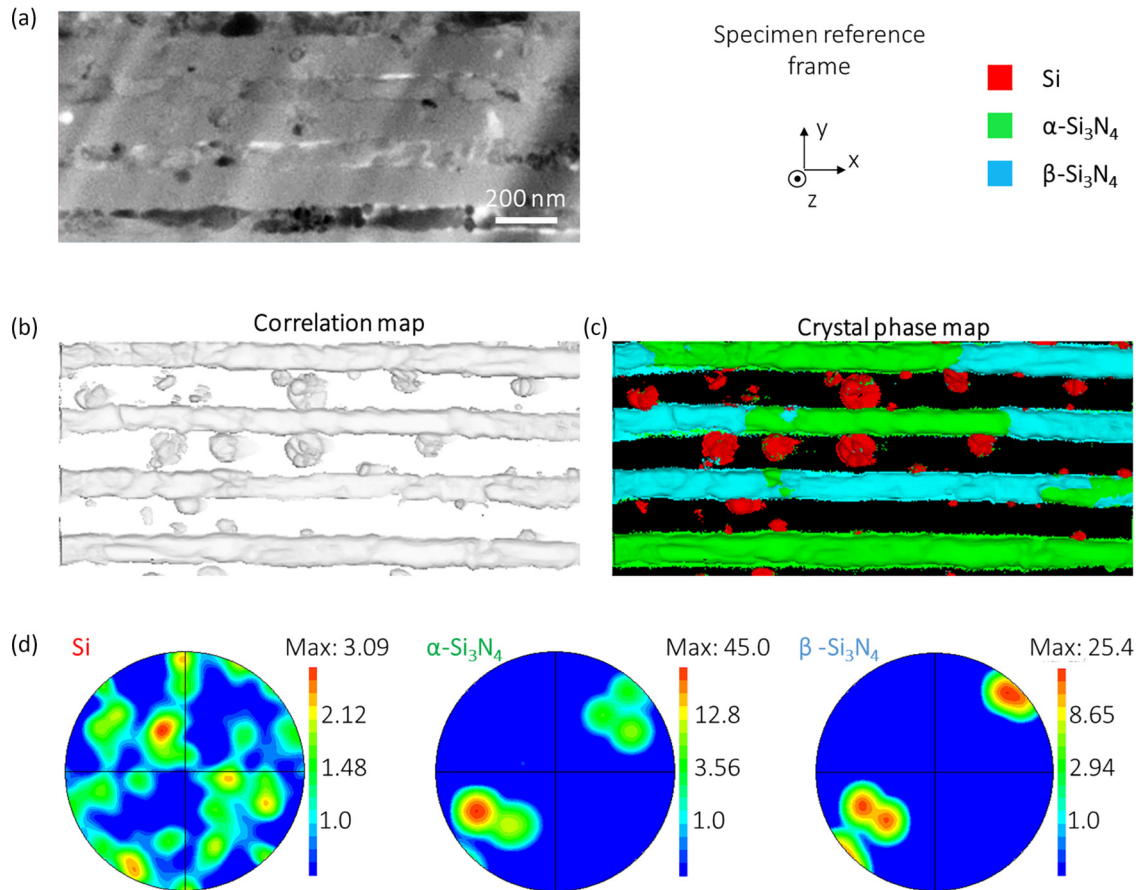


FIG. 6. (a) BF-TEM image of the area selected for Astar-SPED analysis, from the lamellae shown in Fig. 4. The specimen reference frame common to the crystal orientation analysis in the pole figures and the color legend used for phase mapping are shown. (b) Correlation map. The contrast evidences a change of crystal orientation and/or phase. (c) Crystal phase map for the same region, where the colors refer to the legend: diamond Si in red, α -Si₃N₄ in green, and β -Si₃N₄ in blue. Black refers to the nonindexed a-SiO₂ phase. (d) Density plot of the 001 pole figures for each crystal phase, with the color scale representing the specimen area covered with this crystal orientation (in logarithmic scale).

the measured area [23]. It displays contrast-based information about the diffraction patterns changes and thus is a useful tool to evidence the distribution of crystal grains with different orientations and/or phase. Based on the EDS results presented above, crystal phase and orientation mapping were performed considering the presence of d-Si and α , β , and γ polymorphs of Si₃N₄. The map of the crystal phase distribution [see Fig. 6(c)] displays the diamond silicon in red, the α -Si₃N₄ in green, and the β -Si₃N₄ in blue. The presence of spherical crystallites of pure Si within the SiO₂ layers, highlighted by EDS maps in Fig. 5, is confirmed and one can see that the Si crystallites are polycrystalline based on Fig. 6(b). The phases composing the nitride layers are a combination of both α - and β -Si₃N₄, while no γ phase could be observed. This is in line with the literature since the γ phase is known to be formed at high pressures and temperatures [24]. Evidently, although high temperatures were reached during CO laser exposure, the required conditions for the formation of this polymorph were not met. Remarkably, the two Si₃N₄ polymorphs are alternating, with successions of different grains belonging to the same phase extending for several hundreds of nanometers.

The density plots of the 001 pole figures of the different crystal phases are shown in Fig. 6(d). They display a statistical

representation of the crystallites' orientation, extracted from the orientation map visible in Fig. S2 in the Supplemental Material [22]. These figures consist of the stereographic projection of the $\langle 001 \rangle$ crystal orientations of the crystallites in the specimen reference frame; the higher the color scale, the bigger is the area covered by crystallites with this orientation [25]. The pole figures of the α - and β -Si₃N₄ phases show a very strong texture, with the $\langle 001 \rangle$ orientations of all Si₃N₄ crystallites being aligned with the same orientations, whereas the texture of the Si pole figure does not evidence a preferential orientation of the d-Si crystallites, which seems to be randomly oriented. The spatial distribution in the pole figures is comparable between the two different investigated areas (see Fig. S1 in the Supplemental Material [22]).

IV. DISCUSSION

A comparison of the laser-induced modifications between the three explored exposure conditions is proposed in Fig. 7. In the nonlinear absorption regime, at high peak power, ionization of the material takes place and crystalline regions of pure Si are formed within the laser-affected zone, preferentially in the SiN_x layers, as their nonlinear absorption

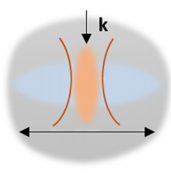
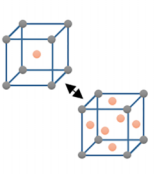
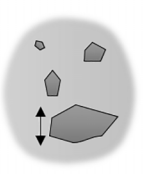
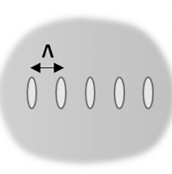
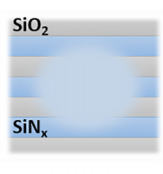

	Extension of the modified zone	Polymorphs in presence	Crystal size range	Self-organization phenomena	Elemental intermixing	Preferential SiN _x layers modification
Femto, 250 kHz, 78 nJ	 1 x 6 μm ²	 Si (in both layers)	 < 50 nm	 Yes (voids)	 Extending out of the focal spot position	 Strong but limited to the edges of the modified zone
Femto, 3 MHz, 16 nJ	1.5 x 5 μm ²	Si (in both layers)	< 50 nm	Not observed	Limited to focal spot position	Strong
CO laser	Several 100s μm along layers	Si (in SiO ₂ layers) α-Si ₃ N ₄ , β-Si ₃ N ₄ (in SiN _x layers)	Si: ≤ layer thickness Si ₃ N ₄ : several 100s μm along layers	Not observed	Not observed	Strong

FIG. 7. Summary of the main laser-induced modification features in multilayers, as observed by TEM, for the three considered exposure cases: femtosecond laser exposure at 250 kHz and 3 MHz, and CO laser exposure.

threshold is lower than the surrounding SiO₂ layers. After exposure to the same laser source, but at higher repetition rates, the confinement effect is stronger at the edges of the modified zone, which show a lower degree of elemental intermixing than the case at low repetition rate. In both cases, however, the area corresponding to the focal spot shows high degrees of elemental intermixing. In the linear absorption regime case, with a mid-IR laser, both layers are affected, but with different outcomes. While a complete phase transition from amorphous to crystalline is observed in the SiN_x layers (specifically resulting in a mix of α- and β-Si₃N₄ phases), a localized and heterogeneously growing Si phase is found in the SiO₂ layers, nested in an amorphous structure.

To support this discussion, a set of relevant structural, mechanical, and thermal properties of both materials is listed in Table I. Some of the values are indicative as they refer to quantities measured in crystalline bulk samples, rather than in amorphous thin films, and may also vary depending on processing conditions, and many values change with environmental conditions such as temperature [26]. Keeping in mind these intrinsic limitations, they offer a starting point for the evaluation of different

materials characteristics and for an initial correlation between materials properties and the first steps of the laser-matter interaction.

In the cumulative regime (hence, high-rate exposure), as the pulse energy is very low (16 nJ), a volume of the material with a transverse dimension smaller than the laser waist is ionized and acts as a heat source. This laser-affected volume is initially discontinuous along the propagation axis, as the SiN_x has a lower ionization threshold than SiO₂. However, from pulse-to-pulse accumulation, the center part gradually heats up and promotes intermixing, while heat is channeled away from the laser-interaction zone. As the SiN_x has a heat conductivity about 20 times higher than SiO₂, the preferred channel of heat conduction is found along the SiN_x layers and explains the stratified contour of the laser-affected volume. SiN_x cannot form a glass phase by melt quenching. The dissociation of SiN_x (characterized by the disappearance of nitrogen in the center part of laser-exposed region) confirms that the temperature went above 1850 °C, a temperature above which Si dissociates from N. The crystallization is therefore induced by the laser at such a low net fluence value thanks to the cumulative heat effect.

TABLE I. Structural, mechanical, and thermal properties of SiO₂ and Si₃N₄.

Physical quantity	SiO ₂	Ref.	Si ₃ N ₄	Ref.
Band gap E_g	9.1 eV	[27]	4.5–6.5 eV	[28]
Refractive index (at $\lambda = 1030$ nm) n	1.45	[29]	1.97 (β)-2.08 (at α)	[30]
Absorption coefficient (at $\lambda = 5$ μm) α	1.91×10^3 m ⁻¹	[15]	11.18×10^3 m ⁻¹	[15]
Permittivity ϵ	4.4	[31]	8.16	[32]
Density ρ	2.20 g cm ⁻³	[33]	3.17 g cm ⁻³	[33]
Young's modulus E	70 GPa	[34]	307 GPa	[34]
Melting temperature T_m	1713 °C	[33]	1900 °C	[33]
Glass transition temperature T_g	~1200 °C	[35,36]	950–1100 °C	[37,38]
Thermal expansion coeff. α_{th}	0.65×10^{-6} K ⁻¹	[34]	2.30×10^{-6} K ⁻¹	[34]
Heat capacity C_p	0.76 J g ⁻¹ K ⁻¹	[19]	0.7 – 0.8 J g ⁻¹ K ⁻¹	[39,40]
Thermal conductivity k	1.4 W m ⁻¹ K ⁻¹	[19]	30 W m ⁻¹ K ⁻¹	[20]
Thermal diffusivity D_T	0.725×10^{-6} m ² s ⁻¹	[41]	8.605×10^{-6} m ² s ⁻¹	[42]

In the CO laser-exposure case, a melt pool formed in the laser-affected region and resulted in the creation of craters. Around these hot spots, the layers heated up to a sufficiently high temperature for crystallization. While SiN_x has a high nucleation and crystallization growth rate, SiO_2 is the opposite and has a very slow crystal growth rate. Away from the melt pool, there is no evidence of strong diffusion of atoms between the two different materials. The crystallization took place as a solid-state transition, with ordering (in the SiN_x layers) and crystal growth (in the SiO_2 layers) occurring without an intermediate melting step *over the whole multilayer volume*. However, given the lower melting temperature of SiO_2 (see Table I), partial melting, or softening, of these layers could, in principle, have happened. In this case, the growth of the crystalline Si phase would be helped by an increased mobility of the ions.

Previous studies on laser-induced crystallization, namely, in the case of femtosecond laser exposure, have been conducted on a variety of oxides [43–49] and suggested the occurrence of crystallization due to a variety of thermal effects. Here, the position of the lamella cut is comprised between 35 and 55 μm from the central position of the focal spot. This means that besides the laser absorption happening *in situ*, the crystallization dynamics is influenced by the heat transfer from the focal spot towards the surrounding volume, after the irradiation, following the thermal gradient, as reported, for example, in [1,50].

The β phase is considered the most stable polymorph of Si_3N_4 and is estimated to be so, up to temperatures above 4000 K [51]. Conversely, the α phase (a low-temperature polymorph) is metastable with respect to the β phase, and is generally formed under certain kinetic conditions, but is later depleted due to the occurrence of a $\alpha \rightarrow \beta$ transition [52,53], at temperatures around 1700 °C [54]. De facto, no $\beta \rightarrow \alpha$ transition has been reported under normal stoichiometric conditions. The occurrence of the amorphous $\rightarrow \alpha$ phase transition has been reported for temperatures between 1150 and 1370 °C, depending on the properties of the starting amorphous material [55], and this reaction is known to possess a lower activation energy than other glass systems based on SiO_2 , at 300 kJ mol^{-1} [54,56].

This transition from the metastable α - Si_3N_4 to the stable β - Si_3N_4 is not evident from our results since we can only analyze the final result of the phase transition process at this specific location and since the ratio between the nitride phases appears to be relatively homogeneous. It should be noted that this area (see Fig. 6) is located on a small lamella, several micrometers away from the focal spot position. It is likely that in the volume between the lamella location and the laser-induced crater [visible in Fig. 4(b)], the α/β ratio fluctuates, representing different stages of the $\alpha \rightarrow \beta$ transition. In the absence of experimental evidence, however, this behavior remains speculative.

Equally of importance is the presence of oxygen at the grain boundaries within the SiN_x layers, as evidenced by EDS imaging, indicating a lower activation energy for diffusion with respect to the $\text{SiO}_2/\text{SiN}_x$ interface. It is also well known that grain boundaries enable a faster diffusion of atomic species due to their larger lattice distortion and defect density [57–59], effectively acting as diffusion highways

across the layers. In a similar dynamics, silicon atoms from the Si-rich SiN_x layers can diffuse towards the SiO_2 layers, as the formation of stoichiometric crystalline Si_3N_4 phases results in the ejection of excess silicon. By moving along the grain and layer boundaries, these atoms are then available for crystal growth within the SiO_2 layers (perhaps promoting the nucleation of crystalline seeds) or for recombination with the oxygen diffusing towards the nitride layers.

Although difficult to analyze dynamically through post-mortem analysis of the laser-exposed areas, the preferential orientation of the Si_3N_4 crystals is remarkably visible from the pole figures and can be correlated with the presence of a thermal gradient, which is oriented along the direction of the layers on the lamella, as indicated in Fig. 4(d). This axis also corresponds to direction x , according to the specimen reference frame indicated in Fig. 6(a). As shown in Table I, silicon nitride has higher values of thermal conductivity and diffusivity, and hence is more affected by the magnitude and orientation of the thermal gradient than the SiO_2 layers. It should also be noted that each SiN_x layer is mechanically constrained by the SiO_2 layers surrounding them and by the rest of the stack. This, coupled with the directionality of the temperature profile, can explain the higher degree of homogeneous crystalline orientations within the nitride phases.

On the other hand, the more diverse orientation distribution of the Si phase can be explained by the formation mechanism of these crystallites. If nucleation is promoted at the layers boundaries, and on defect sites, the orientation of the initial crystal seeds is, in principle, arbitrary. The growth process, especially if occurring in a matrix that is still at least semisolid, also hinders the reorientation of the planes on the short term. As such, the Si crystals coalescence results in the formation of polycrystalline spherical clusters.

There is a noticeable difference between the outputs of femtosecond and CO laser processing. As was reported in previous cases [9], femtosecond laser exposure in the non-cumulative regime shows evidence of energy transfer beyond the focal volume as the affected zone is wider than the laser focusing parameters. This is more noticeable in the case of processing at low repetition rate, suggesting that the introduction of a thermal regime promotes this transfer mechanism. Moreover, femtosecond laser exposure involves the occurrence of material ionization and the generation of shock waves, subjecting the modified material to physical processes that are not commonly seen in studies on phase transitions. The promotion of ionization and the presence of pressure gradients favor the intermixing of elements and the creation of the Si phase, while the prevalence of thermal effects, occurring during cw-laser exposure, does not involve atomic intermixing and results in more homogeneous formation of Si_3N_4 polymorphs. Overall, and as expected, the influence of thermal effects on the modifications is important for both nonlinear and linear absorption cases. However, the larger importance of heat transfer during cw irradiation leads to broader and more pervasive modifications across the multilayer stack, with respect to the femtosecond case. As expected, the exposure time plays an important role, as in the case of CO-laser exposure. Each spot was irradiated for 10 s, which, for the thickness of the layers and the mass of materials considered here, enables usual temperature-driven crystallization processes to happen

thanks to the heat diffusing away from the laser-exposed volume at a slow timescale.

V. CONCLUSIONS

In this study, three different exposure modalities applied to multilayers materials were explored: low- and high-repetition-rate femtosecond processing, which results in local ionization, and continuous-wave CO laser processing, resulting in a purely thermal energy transfer. The role of the ionization process on crystallization and intermixing phenomena was highlighted and examined. A second important parameter was the occurrence, or not, of a thermal regime during laser irradiation, affecting the ability of the sample to dissipate heat during the process.

In the case of femtosecond pulses exposure, there is a difference between nonthermal regimes, as reported in [9], and the thermal regime occurring at high pulse repetition rates. Notably, the modification of the layers is more selective, preferentially targeting the SiN_x layers, due to the different thermomechanical properties of this material with respect to the silicon oxide. The occurrence of periodic voids, reported in the case of low-repetition-rate exposure, is not observed when increasing the pulse density. Moreover, the concentration of nitrogen drops dramatically within the laser-affected area, indicating the presence of an escape pathway enabling the removal of N atoms. However, there are also similarities, as in both cases the crystallization process results in the formation of crystalline Si clusters.

In the case of a continuous-wave CO laser, layer modifications are much larger than the femtosecond case, spanning tens if not hundreds of μm , due to the confocal parameters (which result in a much larger beam) and the thermal nature of the interaction. The focal spot location undergoes partial melting and ablation of the layers, and cracks are observed propagating around the laser-affected area. Surface cross-section analysis indicates the presence of crystallites in the whole multilayer structure. Remarkably, unlike the cases reported in previous chapters, crystallization is observed in

both layers, but with different resulting polymorphs, depending on each layer's composition: in the SiO_2 layers, a heterogeneous crystalline Si phase is nucleated within the amorphous, original material, which then grows into spherical crystallites, pushing the oxygen towards the surrounding volume. In the SiN_x layers, transition from amorphous- SiN_x to a mix of $\alpha\text{-Si}_3\text{N}_4$ and $\beta\text{-Si}_3\text{N}_4$ is observed, with the two competing phases alternating along the layer's length. The orientation of the crystals has been studied and is much less homogeneous in the Si grains than in the Si_3N_4 crystals. The more homogeneous orientation of the nitride phases can be linked to the presence of a thermal gradient during the transition process.

These experiments highlight the key role of ionization processes in defining the nature of the crystalline phases forming during ultrashort pulse laser annealing of multimaterial systems.

More generally and beyond multilayer materials, it further highlights how femtosecond lasers can offer a different pathway to specific crystalline phases in dielectrics, which are not obtained with purely thermally based laser annealing. For instance, in [8] we observed the formation of a pure tellurium phase in a tellurite substrate under femtosecond laser exposure, while a pure thermally based laser annealing yielded another phase.

ACKNOWLEDGMENTS

The authors would like to acknowledge the Swiss National Science Foundation (SNSF) for funding this research through Grant No. CRSII5_180232. R.R. would like to thank S. Benketaf for the development and operation of the CO laser platform setup.

Y.B. and R.R. designed the experiments. R.R. performed the experiments and SEM/TEM characterization of the samples. V.B. performed the SPED analysis of the samples. All authors discussed the experimental results and contributed to the writing of the manuscript. Y.B. designed and supervised the project.

The authors declare no competing interests.

-
- [1] Y. Bellouard, T. Lehnert, J.-E. Bidaux, T. Sidler, R. Clavel, and R. Gotthardt, Local annealing of complex mechanical devices: A new approach for developing monolithic micro-devices, *Mater. Sci. Eng. A* **273**, 795 (1999).
 - [2] G. Torun, A. Romashkina, T. Kishi and Y. Bellouard, Femtosecond laser direct-write photoconductive patterns on tellurite glass, *Phys. Rev. Appl.* **21**, 014008 (2024).
 - [3] A. Salleo, S. T. Taylor, M. C. Martin, W. R. Panero, R. Jeanloz, T. Sands, and F. Y. Genin, Laser-driven formation of a high-pressure phase in amorphous silica, *Nat. Mater.* **2**, 796 (2003).
 - [4] S. Juodkazis, K. Nishimura, S. Tanaka, H. Misawa, E. Gamaly, B. Luther-Davies, L. Hallo, P. Nicolai, and V. Tikhonchuk, Laser-induced microexplosion confined in the bulk of a sapphire crystal: Evidence of multimegabar pressures, *Phys. Rev. Lett.* **96**, 166101 (2006).
 - [5] R. Gattass and E. Mazur, Femtosecond laser micromachining in transparent materials, *Nat. Photon.* **2**, 219 (2008).
 - [6] C. Schaffer, A. Brodeur, J. García, and E. Mazur, Micromachining bulk glass by use of femtosecond laser pulses with nanojoule energy, *Opt. Lett.* **26**, 93 (2001).
 - [7] S. Eaton, H. Zhang, P. Herman, F. Yoshino, L. Shah, J. Bovatsek, and A. Arai, Heat accumulation effects in femtosecond laser-written waveguides with variable repetition rate, *Opt. Express* **13**, 4708 (2005).
 - [8] G. Torun, T. Kishi, D. Pugliese, D. Milanese, and Y. Bellouard, Formation mechanism of elemental Te produced in tellurite glass systems by femtosecond laser irradiation, *Adv. Mater.* **35**, 2210446 (2023).
 - [9] R. Ricca, V. Boureau, and Y. Bellouard, Ultrafast laser interaction with transparent multi-layer $\text{SiO}_2/\text{Si}_3\text{N}_4$ films, *J. Appl. Phys.* **130**, 243105 (2021).
 - [10] R. Ricca and Y. Bellouard, Femtosecond laser-induced confined nanocrystallization in dielectric multilayers, in *Conference on Lasers and Electro-Optics*, Technical Digest Series (Optica Publishing Group, 2022), paper ATu4C.2.

- [11] J. A. Van Vechten, R. Tsu, and F. W. Saris, Nonthermal pulsed laser annealing of Si; plasma annealing, *Phys. Lett. A* **74**, 422 (1979).
- [12] A. Rousse, C. Rischel, S. Fourmaux, I. Uschmann, S. Sebban, G. Grillon, Ph. Balcou, E. Förster, J. P. Geindre, P. Audebert, J. C. Gauthier, and D. Hulin, Non-thermal melting in semiconductors measured at femtosecond resolution, *Nature* **410**, 65 (2001).
- [13] S. K. Sundaram and E. Mazur, Inducing and probing non-thermal transitions in semiconductors using femtosecond laser pulses, *Nat. Mater.* **1**, 217 (2002).
- [14] C. Sheppard, Approximate calculation of the reflection coefficient from a stratified medium, *Pure Appl. Opt.* **4**, 665 (1995).
- [15] J. Kischkat, S. Peters, B. Gruska, M. Semtsiv, M. Chashnikova, M. Klinkmüller, O. Fedosenko, S. Machulik, A. Aleksandrova, G. Monastyrskyi, Y. Flores, and W. Ted Masselink, Mid-infrared optical properties of thin films of aluminum oxide, titanium dioxide, silicon dioxide, aluminum nitride, and silicon nitride, *Appl. Opt.* **51**, 6789 (2012).
- [16] D. Viladot, M. Véron, M. Gemmi, F. Peiró, J. Portillo, S. Estradé, J. Mendoza, N. Llorca-Isern, and S. Nicolopoulos, Orientation and phase mapping in the transmission electron microscope using precession-assisted diffraction spot recognition: State-of-the-art results: Review of pacom (astar) application, *J. Microsc.* **252**, 23 (2013).
- [17] E. F. Rauch and L. Dupuy, Rapid diffraction patterns identification through template matching, *Arch. Metall. Mater.* **50**, 87 (2005).
- [18] C. B. Schaffer, J. F. García, and E. Mazur, Bulk heating of transparent materials using a high-repetition-rate femtosecond laser, *Appl. Phys. A* **76**, 351 (2003).
- [19] K. Ikeda, R. Saperstein, N. Alic, and Y. Fainman, Thermal and kerr nonlinear properties of plasma-deposited silicon nitride/silicon dioxide waveguides, *Opt. Express* **16**, 12987 (2008).
- [20] A. Chojnacka, C. Avedisian, and A. Rendtel, The thermal diffusivity of silicon nitride/silicon carbide nanocomposites using a photothermal deflection technique, *Proc. R. Soc. London, Ser. A* **455**, 2781 (1999).
- [21] J. F. Cannon, Behavior of the elements at high pressures, *J. Phys. Chem. Ref. Data* **3**, 781 (1974).
- [22] See Supplemental Material at <http://link.aps.org/supplemental/10.1103/PhysRevMaterials.8.063402> for additional results.
- [23] A. Kiss, E. Rauch and J. Labar, Highlighting material structure with transmission electron diffraction correlation coefficient maps, *Ultramicroscopy* **163**, 31 (2016).
- [24] J. Jiang, F. Kragh, D. Frost, K. Stahl, and H. Lindelov, Hardness and thermal stability of cubic silicon nitride, *J. Phys.: Condens. Matter* **13**, L515 (2001).
- [25] H. Bunge, *Texture Analysis in Materials Science: Mathematical Methods* (Butterworth, London, 1982).
- [26] D. de Faoite, D. Browne, F. Chang-Díaz, and K. Stanton, A review of the processing, composition, and temperature-dependent mechanical and thermal properties of dielectric technical ceramics, *J. Mater. Sci.* **47**, 4211 (2012).
- [27] V. Astašauskas, A. Bellissimo, P. Kuksa, C. Tomastik, H. Kalbe, and W. Werner, Optical and electronic properties of amorphous silicon dioxide by single and double electron spectroscopy, *J. Electron Spectrosc. Relat. Phenom.* **241**, 146829 (2020).
- [28] S. Ren and W. Ching, Electronic structures of β - and α -Silicon nitride, *Phys. Rev. B* **23**, 5454 (1981).
- [29] I. Malitson, Interspecimen comparison of the refractive index of fused silica, *J. Opt. Soc. Am.* **55**, 1205 (1965).
- [30] Y. Xu and W. Ching, Electronic structure and optical properties of α and β phases of silicon nitride, silicon oxynitride, and with comparison to silicon dioxide, *Phys. Rev. B* **51**, 17379 (1995).
- [31] K. Young and H. Frederikse, Compilation of the static dielectric constant of inorganic solids, *J. Phys. Chem. Ref. Data* **2**, 313 (1973).
- [32] A. Jain, S. Ong, G. Hautier, W. Chen, W. Richards, S. Dacek, S. Cholia, D. Gunter, D. Skinner, G. Ceder, and K. Persson, Commentary: The materials project: A materials genome approach to accelerating materials innovation, *APL Mater.* **1**, 011002 (2013); data retrieved from the Materials Project for Si3N4 (mp-988) from database ver. v2022.10.28.
- [33] Edited by D. R. Lide, *CRC Handbook of Chemistry and Physics* (CRC Press, Boca Raton, FL, 2005).
- [34] S. Pramanik, A. Manna, A. Tripathy, and K. Kar, Current advancements in ceramic matrix composites, in *Composite Materials*, edited by K. K. Kar (Springer, Berlin, Heidelberg, 2017), pp. 457–496.
- [35] B. Champagnon, V. Martinez, C. Martinet, R. Le Parc, and C. Levelut, Density and density fluctuations anomalies of SiO₂ glass: Comparison and light-scattering study, *Philos. Mag.* **87**, 691 (2007).
- [36] P. Richet, GeO₂ vs SiO₂: Glass transitions and thermodynamic properties of polymorphs, *Phys. Chem. Miner.* **17**, 79 (1990).
- [37] T. Lube and J. Dusza, A silicon nitride reference material—A testing program of ESIS TC6, *J. Eur. Ceram. Soc.* **27**, 1203 (2007).
- [38] T. Rouxel, High temperature mechanical behavior of silicon nitride ceramics, *J. Ceram. Soc. Jpn.* **109**, S89 (2001).
- [39] L. Parfen'eva, N. Kartenko, B. Smirnov, I. Smirnov, D. Singh, K. Goretta, H. Misiorek, J. Mucha, D. Wlosewicz, A. Jezowski, and A. Krivchikov, Thermal conductivity and heat capacity of Si₃N₄/BN Fiber Monoliths, *Phys. Solid State* **51**, 2274 (2009).
- [40] H. Ftouni, C. Blanc, D. Tainoff, A. Fefferman, M. Defoort, K. Lulla, J. Richard, E. Collin, and O. Bourgeois, Thermal conductivity of silicon nitride membranes is not sensitive to stress, *Phys. Rev. B* **92**, 125439 (2015).
- [41] C. Clauser, 8.1 The earth's thermal regime, *Renewable Energy* **3C**, 493 (2006).
- [42] O. Koszor, A. Lindemann, F. Davin, and C. Balázs, Observation of thermophysical and tribological properties of CNT reinforced Si₃N₄, *Key Eng. Mater.* **409**, 354 (2009).
- [43] M. Shimizu, M. Sakakura, M. Ohnishi, Y. Shimotsuma, T. Nakaya, K. Miura, and K. Hirao, Mechanism of heat-modification inside a glass after irradiation with high-repetition rate femtosecond laser pulses, *J. Appl. Phys.* **108**, 073533 (2010).
- [44] J. Cao, M. Lancry, F. Brisset, L. Mazerolles, R. Saint-Martin, and B. Poumellec, Femtosecond laser-induced crystallization in glasses: Growth dynamics for orientable nanostructure and nanocrystallization, *Cryst. Grow. Design* **19**, 2189 (2019).
- [45] M. Cavillon, J. Cao, M. Vallet, F. Brisset, L. Mazerolles, B. Dkhil, M. Lancry, and B. Poumellec, Thermal and electron plasma effects on phase separation dynamics induced by ultra-short laser pulses, *Crystals* **12**, 496 (2022).

- [46] X. He, Q. Liu, M. Lancry, F. Brisset, and B. Pommellec, Space-selective control of functional crystals by femtosecond laser: A comparison between SrO-TiO₂-SiO₂ and Li₂O-Nb₂O₅-SiO₂ glasses, *Crystals* **10**, 979 (2020).
- [47] E. Muzi, M. Cavillon, M. Lancry, F. Brisset, R. Que, D. Pugliese, D. Janner, and B. Pommellec, Towards a rationalization of ultrafast laser-induced crystallization in lithium niobium borosilicate glasses: The key role of the scanning speed, *Crystals* **11**, 290 (2021).
- [48] T. Komatsu and T. Honma, Laser patterning and growth mechanism of orientation designed crystals in oxide glasses: A review, *J. Solid State Chem.* **275**, 210 (2019).
- [49] S. Lotarev, A. Lipatiev, T. Lipateva, E. Lopatina, and V. Sigaev, Ultrafast laser-induced crystallization of lead germanate glass, *Crystals* **11**, 193 (2021).
- [50] X. Wang, Y. Bellouard, Z. Xue, and J. J. Vlassak, Thermal modeling of laser-annealing-induced crystallization of amorphous NiTi thin films, *Appl. Phys. A* **90**, 689 (2008).
- [51] R. Dante and C. Kajdas, A review and a fundamental theory of silicon nitride tribochemistry, *Wear* **288**, 27 (2012).
- [52] D. Chen and B. Yu, Pressure-induced phase transition in silicon nitride material, *Chin. Phys. B* **22**, 023104 (2013).
- [53] A. Kuwabara, K. Matsunaga, and I. Tanaka, Lattice dynamics and thermodynamical properties of silicon nitride polymorphs, *Phys. Rev. B* **78**, 064104 (2008).
- [54] Y. Li, L. Wang, S. Yin, F. Yang, and P. Wu, Rapid crystallization process of amorphous silicon nitride, *J. Am. Ceram. Soc.* **94**, 4169 (2011).
- [55] N. Jehanathan, M. Saunders, Y. Liu, and J. Dell, Crystallization of silicon nitride thin films synthesized by plasma-enhanced chemical vapour deposition, *Scr. Mater.* **57**, 739 (2007).
- [56] R. Riedel and M. Seher, Crystallization behaviour of amorphous silicon nitride, *J. Eur. Ceram. Soc.* **7**, 21 (1991).
- [57] G. Gregori, R. Merkle, and J. Maier, Ion conduction and redistribution at grain boundaries in oxide systems, *Prog. Mater. Sci.* **89**, 252 (2017).
- [58] H. Yoshida, Control of high temperature mass transport phenomena through grain boundaries in oxide ceramics based on grain boundary chemical composition and external electric field, *J. Ceram. Soc. Jpn.* **130**, 762 (2022).
- [59] N. Peterson, Diffusion mechanisms and structural effects in grain boundaries, *J. Vac. Sci. Technol. A* **4**, 3066 (1986).